Ground-state degeneracy and complex magnetism of geometrically frustrated Gd$_2$Ir$_{0.97}$Si$_{2.97}$

Sudip Chakraborty [1], Shuvankar Gupta [1], Santanu Pakhira [2,*], Renu Choudhary [2,*], Anis Biswas [2], Yaroslav Mudryk [2], Vitalij K. Pecharsky [2,3], Duane D. Johnson [2,3] and Chandan Mazumdar[1,†]

[1]*Condensed Matter Physics Division, Saha Institute of Nuclear Physics, A CI of Homi Bhabha National Institute, 1/AF Bidhannagar, Kolkata 700064, India*

[2]*Ames National Laboratory, Iowa State University, Ames, Iowa 50011, USA*

[3]*Department of Materials Science & Engineering, Iowa State University, Ames, Iowa 50011, USA*

A new triangular-lattice intermetallic compound Gd$_2$Ir$_{0.97}$Si$_{2.97}$ was successfully synthesized as single phase by deliberately introducing vacancies. Theoretical analysis suggests that the ground state is competing with several low-energy spin configurations due to magnetic frustration on a nearly ideal triangular lattice. Despite a number of competing magnetic states, the compound exhibits long-range antiferromagnetic order at 16 K, a long-range ferrimagnetic transition at 6.5 K, and a reentrant cluster-glass transition below $T_f \sim 3$ K. The complex magnetism in the compound could be correlated with competing antiferromagnetic and ferrimagnetic structures predicted theoretically.

I. INTRODUCTION

Magnetic frustrations in magnetic materials emerge when their intrinsic properties, like topological or geometrical constraints, competing magnetic interactions, lattice geometry, or bond/site disorder, prevent the minimization of the magnetic energy [1–3]. Recently, a large growth of research has emerged on various types of magnetically frustrated systems owing to their unconventional physical properties, viz., formation of spin-ice [4], spin-liquid [5], or spin-glass-type states [6], realization of finite entropy at zero temperature [7], lowering of ordering temperature due to randomness of magnetic interaction [8], arising from ground-state degeneracies [9]. More specifically, geometrically frustrated systems, where antiferromagnetic (AFM) interactions are frustrated by the symmetry of triangular (or tetrahedral) lattice, are of paramount interest as such systems often exhibit unusual electronic and magnetic responses associated with their complex spin textures, along with the strong electron-electron interactions [10–12].

A recent discovery of frustration-led formation of nontrivial topological spin textures in magnetic skyrmions is one such example that is a subject of intense cross-disciplinary research among the fields of physics, material science, and chemistry [13–15]. Initially, such novel spin-texture was evinced in noncentrosymmetric compounds due to the presence of Dzyaloshinskii-Moriya (DM) interactions. In the absence of inversion symmetry, it was shown that magnetic fluctuations driven by geometric frustrations, competing magnetic interactions, and interplay of varying magnetic anisotropy energies play a major role in the formation of nontrivial spin textures in materials [16,17]. Yet, recent observations of such texture—even in a few frustrated centrosymmetric lattice systems—indicate possible alternative mechanism(s) at play.

So far, only a handful of topologically protected skyrmionic systems, almost exclusively Gd-based, are experimentally realized and the fundamental mechanisms that underpin the phenomenon is still not well understood [13,18,19]. The Gd$_2$PdSi$_3$ compound, which adopts a centrosymmetric hexagonal crystal structure (a variant of AlB$_2$-type), is reported to be the first such magnetically frustrated lattice system with evidence of a topological spin state [13]. The compound is a member of a broader R$_2$TX$_3$ family (R = rare earth, T = transition-metal, and X = Si, Ge, In), exhibiting several intriguing properties, including Kondo effects, multiple magnetic transitions, magnetic frustration and spin-glass behaviors, mixed-valence state, large magnetocaloric effects, magnetic memory effects, and bidirectional frequency dependence of dynamical susceptibility [20–28].

In R$_2$TX$_3$ systems, the R ions form an edge-sharing triangular network, where strong magnetic frustration can arise when the nearest-neighbor exchange coupling is AFM. Additionally, crystal geometry-induced magnetic frustrations can also develop due to the presence of competing nearest-neighbor (NN) and next-nearest-neighbor (NNN) exchange interactions because of close values of the hexagonal lattice parameters ($c/a \sim 1$) [22]. Although magnetism in most of the reported members of this series with T = Ni, Cu, Rh, Pd, and Pt (where T-ion magnetic moments are quenched) is governed by Ruderman-Kittel-Kasuya-Yosida (RKKY) interactions between the R-ions localized $4f$ electrons [12,24,29–31], recent studies reveal additional contributions of itinerant moments, when T = Co [32]. The simultaneous presence of RKKY indirect coupling between $4f$-spins via polarization of conduction electrons and the itinerant exchange-derived coupling between the d-electrons and their interplay are expected to add complexity to magnetic phase transitions and associated spin textures. Moreover, such

---

*These authors contributed equally to this work.

†chandan.mazumdar@saha.ac.in

complex interplay of local and itinerant magnetism can also have a pivotal role in stabilizing nanoscale topological spin states [13,33].

Although there are many studies describing centrosymmetric R_2TX_3 systems containing $3d$ and $4d$ transition metals, less information is available for systems with $5d$ metals, except for T = Pt. Compared to $3d$ and $4d$ transition-metal systems, the introduction of $5d$ transition-metals is expected to significantly alter the magnetic interactions due to their strong spin-orbit coupling. Additionally, the wider $5d$ transition-metal bandwidth may also result in hybridization with rare-earth $5d$ band, further affecting f-d interactions.

Here, we report the formation of a novel centrosymmetric R_2TX_3-type compound containing $5d$-transition metal, $Gd_2Ir_{0.97}Si_{2.97}$ and study its unconventional magnetic properties. We have shown that the compound is a geometrically frustrated system that undergoes multiple magnetic transitions at low temperatures associated with different spin configurations and competing energies.

II. METHODS

A. Experimental details

The polycrystalline Gd_2IrSi_3 and $Gd_2Ir_{0.97}Si_{2.97}$ samples of approximately 3 g each were prepared by using standard arc melting procedure. Pure (>99.9 wt.%, Alfa Aesar, USA) starting elements were weighed in nominal stoichiometric ratios and arc-melted together in an inert argon atmosphere on a water-cooled copper hearth. The ingots were remelted five times, flipping them over after each melting to improve chemical homogeneity. Weight losses after melting were negligible (<0.5%). Parts of each sample were wrapped in a Ta-foil and annealed under vacuum at 1073 K for seven days. Powder x-ray diffraction (XRD) measurements of as-cast and annealed samples were carried out in a commercial powder diffractometer using Cu-K$_\alpha$ source (rotating anode, 9 kW, Model: TTRAX-III, Rigaku Corp., Japan). Full Rietveld analysis of the obtained XRD spectra were done using FULLPROF [34]. The sample homogeneity and chemical compositions were confirmed using a JEOL scanning-electron microscope (SEM) equipped with an energy-dispersive x-ray spectroscopy (EDS) analyzer.

A SQUID magnetometer (Quantum Design Inc., USA) was employed to study magnetic properties in the temperature range 2–300 K and magnetic field ranging from 0 to 70 kOe. Both zero field-cooled (ZFC) and field-cooled (FC) protocols were adopted for magnetic susceptibility measurements. In ZFC procedure, a sample was cooled to the lowest temperature (2 K) without the application of any external magnetic field and then magnetization measurements were carried out in a specified magnetic field during heating from 2 to 300 K. In FC protocol, a sample was cooled to the lowest temperature under an applied magnetic field and the magnetization (M) versus temperature (T) data were collected in the same field during heating. Measurements during cooling in the same field (FCC) were practically indistinguishable from those performed during heating after FC. Isothermal magnetic-field dependencies of magnetization, M versus H, were measured at different temperatures. Before every set of M-H measurements, the sample was cooled down to the spec-

ified temperature from a temperature well above the highest transition temperature in the absence of magnetic field. AC susceptibility measurements were performed under an excitation field of 6 Oe with frequency ranging from 1 to 1489 Hz.

Heat capacity measurements were performed using a commercial Physical Property Measurement System (PPMS, Quantum Design Inc., USA) using the relaxation technique in the temperature range 2–300 K and magnetic fields ranging from 0 to 70 kOe. Electrical resistivity measurements were implemented in a standard four probe technique in the same PPMS set up. A rectangular shaped sample was cut and polished for this purpose and silver epoxy was used for making electrical connections.

B. Computational methods

Density-functional theory (DFT) was used to calculate the ground-state energy and magnetic properties of the Gd_2IrSi_3 system using a projector augmented wave (PAW) method [35] as implemented in the Vienna Ab initio Simulation Package (VASP) [36]. For the exchange and correlation functional, the Perdew-Burke-Ernzerhof based generalized gradient approximation (PBE-GGA) [37] is used. We applied spin-orbit coupling (SOC) and an onsite electron-correlation (effective Hubbard) parameter $|U - J|$ of 6 eV for proper placement of Gd-$4f$ states. The room-temperature lattice parameters (Table I) are used as inputs in DFT calculations. The total-energy convergence criterion for the self-consistent calculations is 10^{-7} eV per cell, using an energy cutoff of 520 eV for the wave functions. The Brillouin-zone integration was performed using a k-point mesh based on the tetrahedron method with Bloch corrections. A Γ-centered grid of $12 \times 12 \times 12$ k-points was used for Brillouin-zone sampling.

III. RESULTS

A. Structural characterization

Majority of R_2TSi_3 compounds are reported to crystallize in a hexagonal AlB_2-type structure or a derivatives [12,24,38]. In the AlB_2 prototype structure *(P6/mmm)*, lattice parameters

TABLE I. Crystallographic parameters of $Gd_2Ir_{0.97}Si_{2.97}$ obtained by full Rietveld refinement of room-temperature powder XRD data.

Compound	$Gd_2Ir_{0.97}Si_{2.97}$				
Crystal Structure	Er_2RhSi_3 type: derived from AlB_2 type Structure				
Space group	*P6₃/mmc, No. 194*				
$a = b$	8.156(1) Å				
c	8.037(7) Å				
Atomic coordinates					
Atom	Wyckoff position	x	y	z	Occupancy
Gd1	2b	0	0	1/4	1
Gd2	6h	0.5049	−0.5049	1/4	1
Ir	4f	1/3	2/3	0.0214	0.965(2)
Si	12k	0.1543	0.3087	0.0023	0.981(1)

a and *c* are similar in value; here the atoms at Al site and those at B sites are arranged in alternating layers. In the simplest structure for R_2TX_3 compounds, R atoms occupy Al positions, while T and X atoms are randomly distributed in B positions. Doubling the unit cell edges (*a*) leads to an ordered variant of the Ce_2CoSi_3-type structure, where T and X atoms occupy distinct crystallographic Wyckoff sites (2*d* and 6*m*) and R atoms occupy two different Wyckoff sites (1*a* and 3*f*). This structural modification retains the same space group $P6/mmm$. R_2PtSi_3 and R_2CoSi_3 are known to form this crystal structure type [30,32]. A third variant, R_2RhSi_3, is yet another derivative of the AlB_2-type, where both *a* and *c* parameters are doubled compared to the parent [38]. The exact description of this crystal structure (known as the Er_2RhSi_3-type) remains somewhat disputed, as both $P6_3/mmc$ and $P\bar{6}2c$ could describe the structure quite well [39]. In both cases, R atoms occupy two different sites in 1:3 ratio, while Rh and Si atoms occupy two distinct Wyckoff positions. Ce_2IrSi_3 [40], the only known compound in the R_2IrSi_3-series, was reported to crystallize in the Ce_2CoSi_3-type crystal structure.

The room-temperature XRD patterns of Gd_2IrSi_3 and $Gd_2Ir_{0.97}Si_{2.97}$ materials are shown in Fig. 1(a). Although majority of the Bragg peaks of the stoichiometric Gd_2IrSi_3 could be indexed assuming the Ce_2CoSi_3-type structure, a few of them remain unindexed. Assuming the Er_2RhSi_3-type structure helps to account for some of these unindexed peaks, yet a few are still unaccounted. It is known that many polycrystalline R_2TX_3-type compounds do not form at ideal 2:1:3 stoichiometries, and contain RTX_2 [21,32] or RT_2X_2 secondary phases [41]. Accordingly, Rietveld refinement of the XRD pattern of Gd_2IrSi_3 [Fig. 1(a), top] confirms that the stoichiometric sample contains the R_2RhSi_3-type as the main phase coexisting with 6 wt.% of $GdIrSi_2$ as impurity. Annealing the sample at 1073 K for seven days has no effect on the phase fractions at all.

As reported, single phase R_2TSi_3 materials can be obtained by introducing defects both on the T and Si sites [20,21,26,32,42–44]. Considering this, we have also synthesized an off-stoichiometric composition $Gd_2Ir_{0.97}Si_{2.97}$. All of the Bragg peaks in the XRD pattern of this off-stoichiometric composition [see Fig. 1(a), bottom] are fully indexed with the Er_2RhSi_3-type structure [38], within the accuracy of the experiment confirming the single-phase nature of $Gd_2Ir_{0.97}Si_{2.97}$. Annealing at 1073 K has not effect on the XRD pattern, likely indicating that the compound melts congruently.

Rietveld refinement results are presented in Table I. This particular atomic arrangement leads to three closely spaced Gd-Gd distances: Gd(1)-Gd(1) = 4.018(3) Å, Gd(2)-Gd(2) = 3.965(2) Å, and Gd(1)-Gd(2) = 4.078(2) Å. This feature may have a profound influence on the compound's magnetic properties, because similar but different Gd-Gd distances could result in competing magnetic interactions, often seen in many compounds with unconventional magnetic ground states. We will elaborate on this point later while discussing magnetic properties of the sample. Scanning electron microscopy (SEM) and energy-dispersive x-ray (EDX) spectroscopy measurements were carried out on $Gd_2Ir_{0.97}Si_{2.97}$ and the compound was found to be homogeneous in nature. The elemental composition obtained from EDX measurement
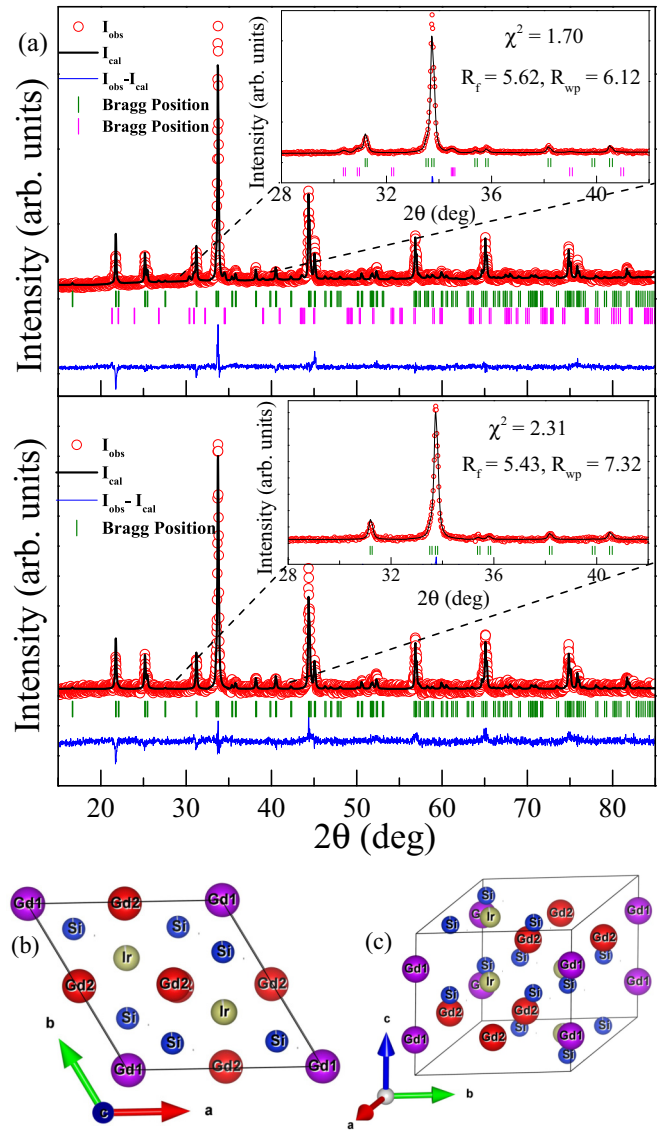

FIG. 1. (a) XRD patterns of (top) Gd_2IrSi_3 and (bottom) $Gd_2Ir_{0.97}Si_{2.97}$İn (top) the green bars indicate calculated Bragg peak positions for the R_2RhSi_3-type main phase, while magenta bars are Bragg peak positions for the $GdIrSi_2$ impurity. Insets illustrate regions that highlight presence (top) and absence (bottom) of Bragg peaks of the impurity. (b) Crystallographic representation of $Gd_2Ir_{0.97}Si_{2.97}$ unit cell in the *ab* plane, showing the hexagonal network of Gd atoms. (c) Unit cell of the studied compound.

at multiple spots is $Gd_2Ir_{0.94(3)}Si_{2.96(3)}$, which matches both our starting composition and stoichiometry determined from the Rietveld refinement within error bars.

B. DC magnetization study

DC magnetic susceptibility ($\chi = M/H$) of $Gd_2Ir_{0.97}Si_{2.97}$ measured in both ZFC and FC protocols in a 100 Oe applied magnetic field is shown in Fig. 2. Three distinct anomalies are seen at ∼120 K, ∼16 K, and ∼6.5 K. The peak at 16 K remains stable both in the ZFC and FC measurements, also in fields of 5 kOe and lower (Fig. 3), and hence can be considered
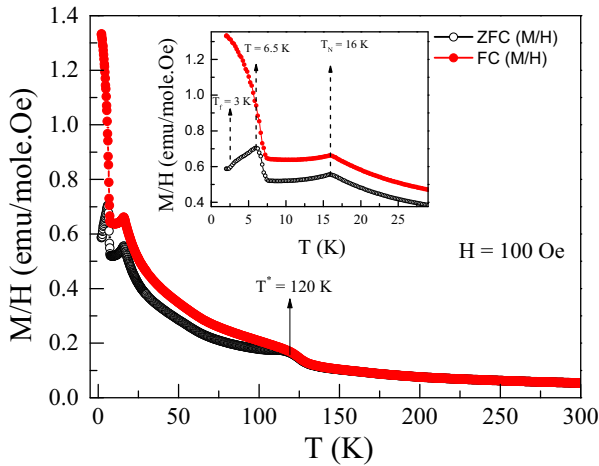
FIG. 2. DC magnetic susceptibility vs temperature measured in a 100 Oe applied magnetic field.

FIG. 4. Inverse DC susceptibility plot at various applied magnetic fields.

as the signature of AFM type transition. However, although the susceptibility under ZFC protocol decreases below 6.5 K, the FC measurement exhibits a ferromagnetic (FM)-like increase, suggesting a development of an FM component or a metastable phase below 6.5 K. An additional weak feature is barely discernible around 3 K in the ZFC data. This feature would be discussed in more detail in connection with AC susceptibility behavior later (Sec. III D).

In addition to these low-temperature anomalies, a broad maximum is observed around 120 K where irreversibility between ZFC and FC data starts to manifest (Fig. 2). With an increase in externally applied field, that maximum at
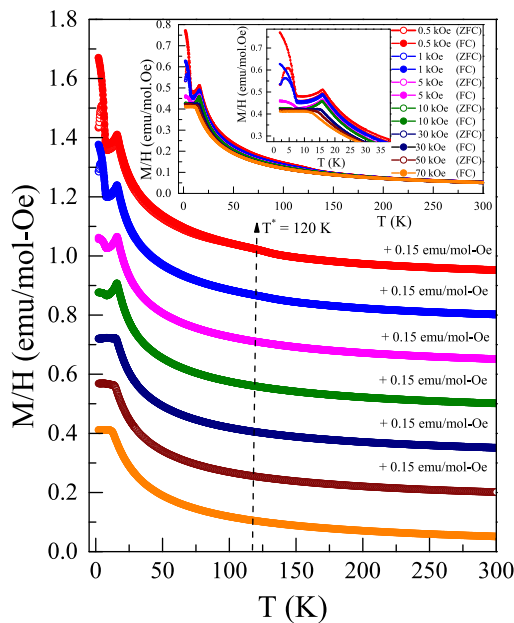

FIG. 3. DC magnetic susceptibility vs temperature measured in various applied magnetic fields. Susceptibilities measured under different fields are presented in a shifted scale (0.15 emu/mol-Oe for measurements under each field) along the *y* axis. Inset shows actual view of magnetic susceptibility.
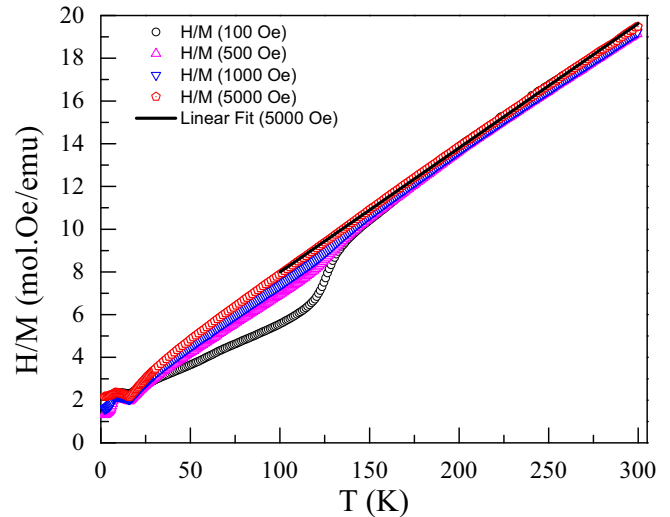
120 K flattens and the magnetic irreversibility diminishes. For H $\geqslant$ 5 kOe, the irreversibility as well as the maximum completely disappear and the magnetic susceptibility appears to be paramagnetic-like over a much larger temperature region, $16 < T < 300$ K (Figs. 3 and 4). Such a feature in magnetic susceptibility is akin to the presence of a weak FM-like interactions that manifest only in low-field measurements, but are buried in the enhanced paramagnetic susceptibility when the external magnetic field strength is increased. In the present case, a rather moderate field of 5 kOe appears to be sufficiently strong to suppress such FM interactions. Such behavior may be reflective of either a small magnetic impurity or it may be intrinsic to the main phase. An impurity, if present, must be beyond the detection limit of our XRD/EDX results combined with SEM image analysis. We also note that a similar anomaly around the same temperature was also reported in a structurally related $Pr_2Co_{0.86}Si_{2.88}$, where the feature was assumed intrinsic to the main phase, originating from the ordering of weak Co-spins [32]. In the case of $Tb_{5-x}La_xSi_2Ge_2$, it was shown that replacing a small fraction of Tb atoms with nonmagnetic La ($x = 0.075$) may result in formation of short-range ferromagnetic clusters and Griffiths-phase characteristics at $T_G = 190$ K and $T_{G*} = 156$ K [45]. Considering all of the above, our magnetic susceptibility measurement (Fig. 2) most likely reflects the presence of a similar Griffiths-phase like behavior in a nonstoichiometric sample with nominal composition $Gd_2Ir_{0.97}Si_{2.97}$.

As illustrated in Fig. 3, the anomaly at ∼16 K shifts to low temperatures with the application of magnetic field greater than 10 kOe. This is typical for most of AFM materials and indicates that the AFM spin arrangement remains quite robust up to this field. In contrast, interactions that support anomaly at ∼6.5 K appear to be quite weak, as the anomaly disappears for $H > 5$ kOe. Considering all these features together, the magnetic ground state appears to be quite delicate in character, as often found in many magnetically frustrated systems. This type of behavior is also in agreement with the theoretical model discussed later (Sec. III F).
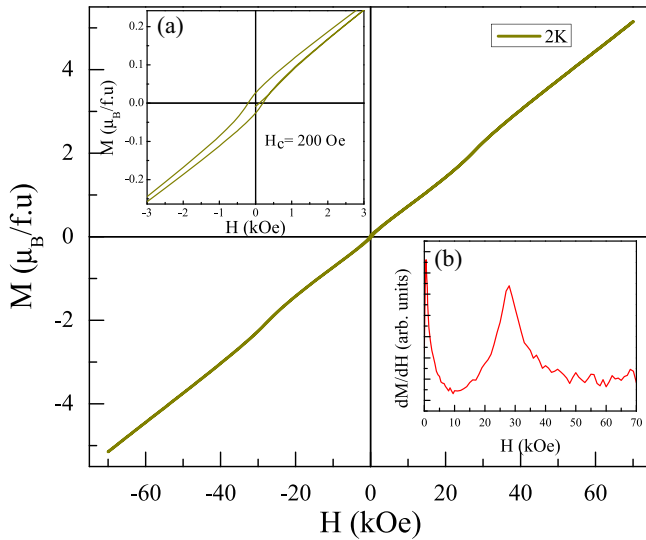
FIG. 5. Isothermal magnetization measured at $T = 2$ K, Inset (a) highlights hysteresis at low temperature, inset (b) represents dM/dH as a function of magnetic field.

The inverse susceptibilities displayed in Fig. 4 at different magnetic fields, along with the Curie-Weiss fit [46] of the data measured in a 5 kOe magnetic field above 100 K. The fitting yields the effective moment $\mu_{\mathrm{eff}} = 11.73$ μ_B/f.u. and Weiss temperature $\theta_p = -37$ K. Assuming the moment is associated with rare-earth Gd ion only, as found in most of the rare-earth intermetallic systems, this corresponds to 8.29 μ_B/ Gd^{3+} ion, which is slightly higher than the expected $g_J\sqrt{[J(J+1)]} = 7.94$ μ_B/Gd, where g_J is the Lande factor and J is total angular momentum of noninteracting Gd^{3+} ions [24]. This slightly higher than theoretical μ_{eff} is common, suggesting additional contributions from $5d$ electrons of either or both Gd and Ir [47–50]. The AFM ground state is further confirmed by the negative value of the Weiss temperature ($\theta_p \sim -37$ K). Additionally, a rather large value of frustration parameter, $f = |\theta_p|/T_N \sim 2.5$, points to an appreciable magnetic frustration in the system [51,52].
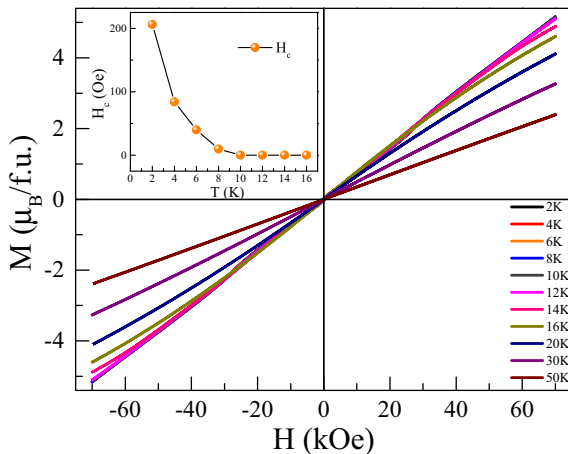

FIG. 6. Magnetic field dependence of magnetization at various temperatures with the inset illustrating temperature dependence of hysteresis.
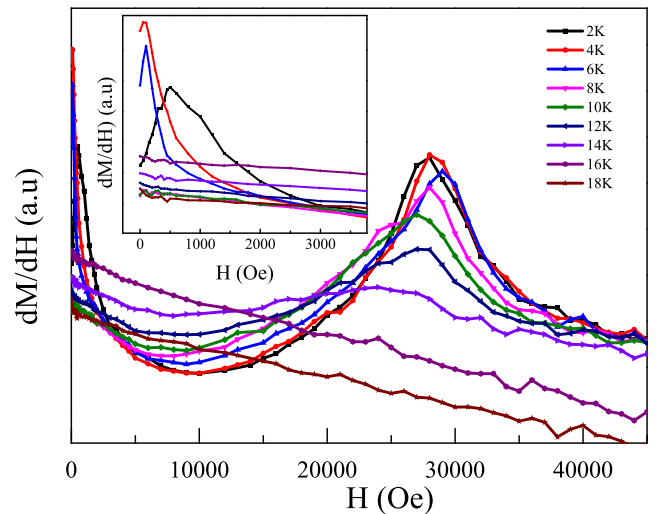

FIG. 7. dM/dH at different temperatures. Inset shows an expanded view of the low-field region.

The $M(H)$ behavior remains almost linear for $T < 12$ K, as expected for AFM systems (Figs. 5 and 6) [53,54]. However, a close look at the low-temperature $M(H)$ data near $H = 0$ shows minor hysteresis behavior [Fig. 5(a)]. Weak coercivity at low temperatures indicates presence of a magnetic phase which could be either glassy or weakly ferromagnetic in character. As the temperature increases, the hysteresis vanishes above 8 K, and $M(H)$ becomes more distinctly linear. At 2 K, dM/dH reveals two peaks: at $\sim$500 Oe and 28 kOe [Fig. 5(b)], suggesting field-induced spin-reorientations. As the measurement temperature increases, the low-field dM/dH anomaly extends only up to 6 K. In contrast, the dM/dH peak at $\sim$28 kOe is quite robust and it persists till $\sim$14 K (Fig. 7) irrespective of different magnetic spin arrangement regions, viz., $2 < T < 6.5$ K or AFM-type in $6.5 < T < 16$ K.

C. Heat capacity study

Heat capacity behavior (Fig. 8) is shown in the temperature range 2–300 K measured in the absence of external magnetic field. A pronounced λ-type peak at $T\sim16$ K confirms the long-range nature of magnetic ordering. An additional weak anomaly, visible around $T \sim 6.5$ K is also consistent with the magnetic susceptibility data. The heat capacity at room temperature is $\sim$146 J/mol-K is in a good agreement with the classical Dulong-Petit limit, C = $3n$R ($\sim$148.15 J/mol-K), where R is the universal gas constant, and n is the number of atoms per formula unit (f.u.), here $n = 2 + 0.97 + 2.97 = 5.94$.

The lattice heat capacity of $Gd_2Ir_{0.97}Si_{2.97}$ cannot be represented by a Debye model with a single Debye temperature (θ_D) in the measured temperature range. This is primarily because the Debye model is only applicable at high temperatures ($T > \theta_D/10$) or at low temperatures ($T < \theta_D/50$), but not in the intermediate temperature region [56]. Therefore, it is a common practice to use a combination of Debye and Einstein models to describe the temperature dependence of heat capacity [57–61]. The sum of electronic and lattice contributions to
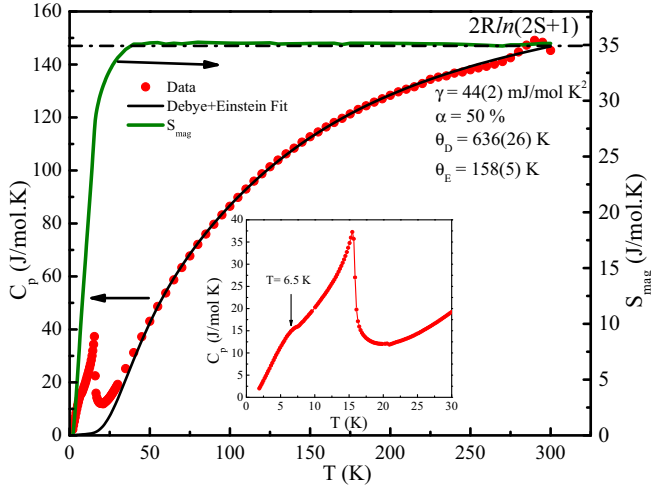
FIG. 8. Zero-field heat capacity data of $Gd_2Ir_{0.97}Si_{2.97}$. Debye+Einstein fitting is denoted by black line and magnetic entropy is denoted by olive line. Inset shows the expanded view in the magnetic-ordering region between 0 and 30 K. The hump in the experimental data around $\sim$290 K is due to melting of Apiezon N grease used [55].

the heat capacity is thus defined as

$$C_P = \gamma T + \alpha C_D(T) + (1-\alpha)C_E(T), \qquad (1)$$

where the Debye contribution is

$$C_D = 9N_D R \left(\frac{T}{\theta_D}\right)^3 \int_0^{\frac{\theta_D}{T}} \frac{x^2 e^x dx}{[e^x-1]^2}, \qquad (2)$$

and similarly the Einstein contribution is

$$C_E = 3N_E R \frac{x^2 e^x}{[e^x-1]^2}, \qquad (3)$$

In Eq. (1), γ is the Sommerfeld coefficient, N_D and N_E are the number of Debye and Einstein oscillators, respectively, and α is a relative weight of the heat capacity in the Debye approximation. In Eq. (3), $x = \theta_E/T$, where θ_E is the Einstein temperature. In our analysis, $C_p(T)$ can be described well in the entire temperature range by considering equally weighted Debye and Einstein contributions, and thus Eq. (1) can be simplified as

$$C_P = \gamma T + \frac{1}{2}[C_D(T) + C_E(T)]. \qquad (4)$$

The best match of experimental data in the range 35–300 K to Eq. (1) yields $\gamma = 44$ mJ/mole-K^2, $\theta_D = 636$ K, and $\theta_E = 158$ K. The value of θ_D obtained from our analysis appears to be on the higher side of those reported for majority of known intermetallic systems; yet a significant number of compounds do show even much larger θ_D [57,58,62–64], suggesting rather enhanced hardness of those materials. Of course, it may also be mentioned here that fitting over the whole temperature region 2 < T < 300 K) could also overestimate θ_D, as the Debye model applies to low-frequency modes of lattice vibration (acoustic modes). This is true only in the low-temperature region, as the heat capacity data at the high-temperature region involves the high-frequency (optical) modes as well. This
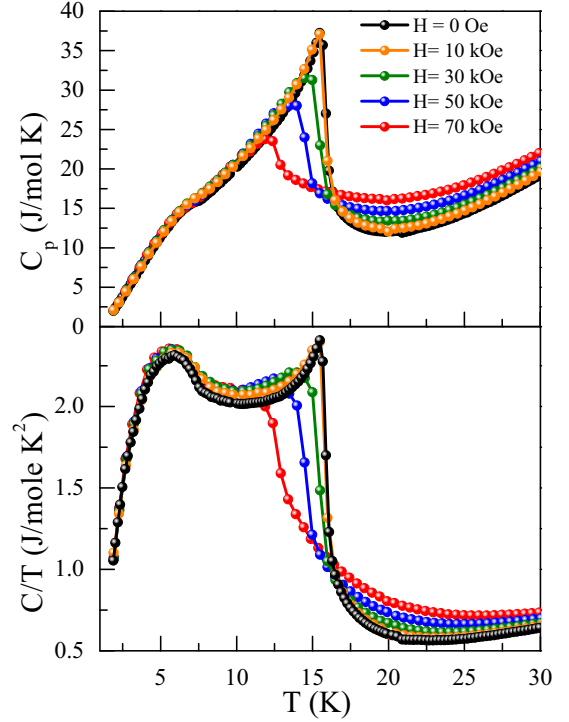

FIG. 9. Upper panel shows field-dependent heat capacity up to 70 kOe; lower panel shows C_p/T data at different fields.

consideration is also known to affect the value of θ_D obtained from heat-capacity analysis [56,65].

Typically, the magnetic contribution to the heat capacity is calculated by subtracting the lattice and electronic heat capacity of a nonmagnetic analog. In the absence of data of La or Y analoges, we use the fit described in Eq. (4) extrapolated to the low-temperature region to estimate the combined contribution of C_{el} and C_{ph} in the magnetically ordered state. Taking $C_{mag} = C_p - (C_{el} + C_{ph})$, and integrating C_{mag}/T over the whole temperature region, the magnetic entropy at $T_N = 16$ K is thus estimated to be $S_{mag} = 14.4$ J/mol-K per Gd^{3+} ion, which is 80.5% of the theoretical total magnetic entropy value $Rln(2J+1) = 17.38$ J/mol-K per Gd^{3+} ion with S = 7/2 and L = 0 [66]. Magnetic entropy is fully removed around $T = 35$ K (Fig. 8). This suggests the presence of dynamic short-ranged magnetic correlations in the system up to 35 K, similar to that observed for other Gd-based compounds [54,67]. Presence of such short-ranged magnetic correlations is also responsible for the reduced magnetic entropy at T_N.

Applying external magnetic fields up to 70 kOe (Fig. 9) gradually shifts the peak at T_N toward lower temperatures ($\sim$11 K for H = 70 kOe), while the corresponding magnetic entropy is getting redistributed toward the high-temperature region. This is a typical behavior of many AFM systems [68–70], where long-range order is disturbed by the application of external field, but short-ranged correlations develop at higher temperatures. However, the anomaly at $\sim$6.5 K remains invariant under application of magnetic field. This suggests that observed low-temperature anomaly could be a result of Schottky-like effect [66,69]. We will further discuss this possibility in Sec. III G.
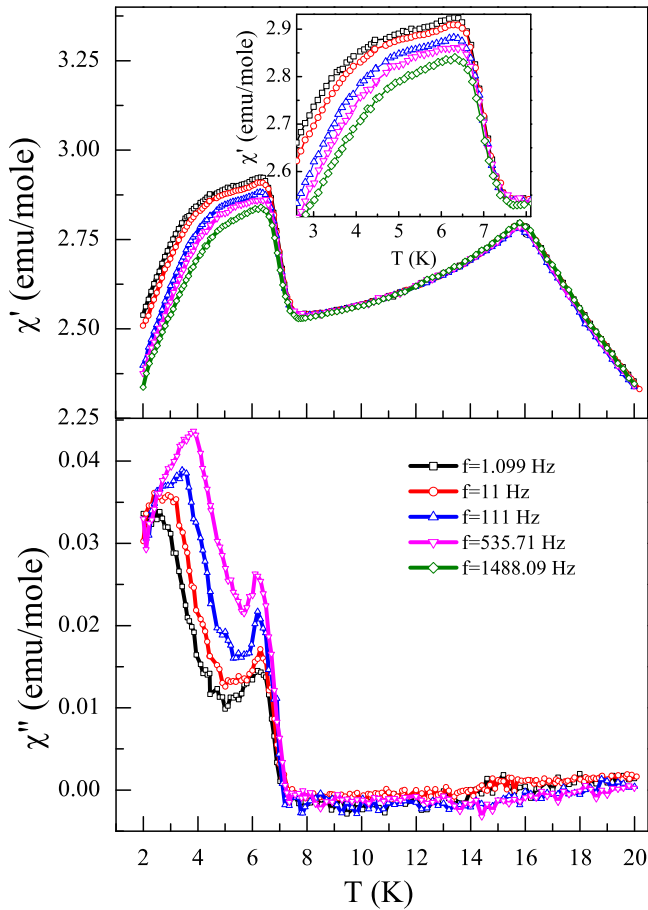
FIG. 10. (Top) Temperature variation of the real part of AC magnetic susceptibility data and (bottom) the imaginary part (loss component). Inset shows the expanded view of the real part of low-temperature AC susceptibility. $\chi''(T)$ data for $f = 1488.09$ Hz not shown because of excessive scatter due to measurement limitation.

FIG. 11. The temperature variation of imaginary part of AC magnetic susceptibility of $Gd_2Ir_{0.97}Si_{2.97}$ at different applied frequencies. The dashed arrow serves only as a guide to eye, passing close to the peak temperatures of $\chi''(T)$ measured at different frequencies. The inset (a) shows the plot of $\log(\tau)$ vs $\log(t)$ and inset (b) is the graphical representation of the Vogel-Fulcher law. The solid lines in both insets (a) and (b) are the linear fits of the two curves.

D. AC magnetic susceptibility

Consistent with DC data of Fig. 2, the real component of AC susceptibility, $\chi'(T)$, presented in Fig. 10, shows a peak around 16 K. As the temperature decreases, a sharp jump in $\chi'(T)$ is observed below ~ 7.5 K, reaching a maximum at ~ 6.5 K. As the temperature is lowered further, a shoulder appears at ~ 4.5 K. Above 7.5 K, $\chi'(T)$ shows no discernible frequency dependence, including the peak at ~ 16.5 K, suggesting that the magnetic order between 7.5 and 16.5 K is of long-range nature. The imaginary part, $\chi''(T)$, representing the loss component in this temperature range is nearly zero, suggesting lack of domains consistent with AFM order [25,61]. The AC magnetic susceptibility (data not shown) also exhibits a broad anomaly around 120 K, mimicking the behavior of DC magnetic susceptibility; the anomaly vanishes in bias DC fields exceeding 500 Oe.

Conversely, a clear signature of magnetic domain formation (either ferromagnetic or ferrimagnetic) is evident in $\chi''(T)$ data below 7.5 K, which eventually gives rise to a maximum around 6.5 K. While $\chi'(T)$ remains almost unchanged in various frequencies in the temperature region above the peak $(6.5 < T < 7.5$ K$)$, frequency-dependent change in
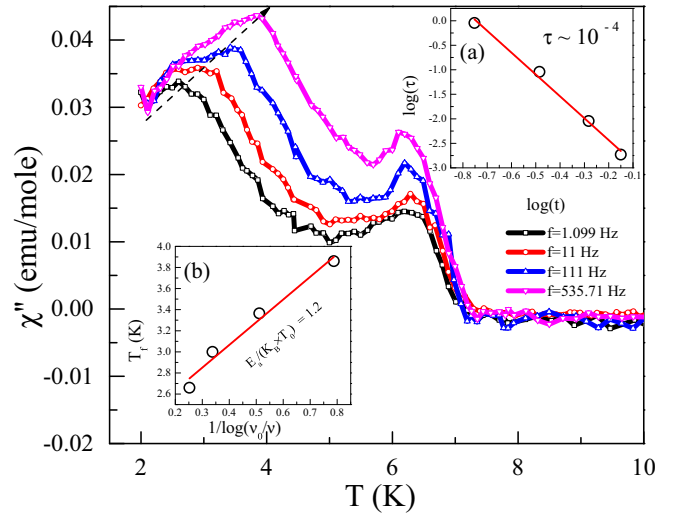
magnitude of $\chi'(T)$ is clearly seen below the peak temperature ~ 6.5 K. Such frequency-dependent AC-susceptibility behavior around ~ 6.5 K is a strong indication of the emergence of a metastable magnetic state [71,72]. At the same time, the frequency independence of the peak temperature in both $\chi'(T)$ and $\chi''(T)$ also suggests a modification of magnetic structure around ~ 6.5 K which remains long range.

As the temperature is reduced below 6.5 K, $\chi''(T)$ initially decreases and then begins to increase peaking at ~ 3 K for $f = 1.099$ Hz. As the frequency increases, this peak shifts toward higher temperature region, reaching 3.8 K for $f = 535.71$ Hz. Such shift in peak in $\chi''(T, f)$ is an indication of a glassy state in the compound [24,57]; the shift is unresolved in $\chi'(T, f)$ data as the change in overall long-range magnetic structure around ~ 6.5 K hides the manifestation of a glassy phase. However, the absence of any frequency dependence of both $\chi'(T, f)$ and $\chi''(T, f)$ behavior above ~ 6.5 K clearly suggests that the development of a glassy state is related to the change/development in magnetic structure around ~ 6.5 K. It, therefore, appears to be highly plausible that metastability appearing around ~ 6.5 K is a precursor of the glassy state observed below ~ 4 K [73]. In other words, the system most likely undergoes a reentrant glassy behavior at low temperature. The presence of a glassy phase is also highly possible in this system because theoretical calculation (Sec. III F) indicate different magnetic configurations of nearly equal energy. It is a competition between ferrimagnetic (FiM), FM, and AFM ground states that is the likely origin of magnetic frustration and metastability in the system that leads to glassy phase at low temperature.

To understand the nature of this magnetically glassy state, we turn to frequency-dependent peak shift of $\chi''(T, f)$ around 4 K (Fig. 11). The peak position shifts from 3.03 K at 1 Hz to 3.87 K at 535.71 Hz. Similar behavior is observed in many

magnetically glassy systems where the shift in relative spin freezing temperature per decade is defined as [57,74,75]

$$\delta T_f = \frac{\Delta T_f}{T_f \Delta(\log_{10} f)}. \tag{5}$$

Here, f is the applied frequency and T_f is the freezing temperature. Using Eq. (5), δT_f is ~0.08, which is relatively high for a canonical spin-glass system but matches closely with those reported for cluster glasses [24,74,76]. The cluster-glass nature could be further confirmed through the dynamical scaling hypothesis according to which the relaxation time at a particular frequency at spin freezing temperature, T_f, is related to spin-spin correlation length, ξ, as $\tau \propto \xi^z$. It follows the general relation

$$\tau = \tau_0 \left(\frac{T_f - T_{SG}}{T_{SG}} \right)^{-z\nu'}, \tag{6}$$

where $\tau = f^{-1}$ is the relaxation time at a particular applied frequency, and τ_0 is the relaxation time for a single spin flip. T_{SG} is the spin freezing temperature at $f = 0$ Hz. $z\nu'$ is known as the critical exponent for correlation length $\xi = (\frac{T_f}{T_{SG}} - 1)^{-\nu'}$. The dynamical critical exponent $z\nu'$ normally varies between 4 and 12 in a glassy system. Using Eq. (6), $z\nu'$ is 4.46, which confirms the presence of a glassy phase, whereas the estimated $\tau_0 \sim 10^{-4}$ s is much greater when compared to canonical spin glasses (10^{-9}–10^{-15} s) [74,75]. The estimated value of τ_0 in $Gd_2Ir_{0.97}Si_{2.97}$ matches those of cluster-glass systems [24,57,77].

The frequency variation was also analyzed using the Vogel-Fulcher law, where the frequency dependence is described as

$$f = f_0 \exp \left[-\frac{E_a}{k_B(T_f - T_0)} \right]. \tag{7}$$

Here f_0 is the characteristics frequency, T_0 is the Vogel-Fulcher temperature, E_a is the activation energy, and k_B is the Boltzmann constant. From the fitting, $E_a/k_B T_0 = 1.2$. For canonical spin-glass systems, this value is generally found to be much smaller than 1, whereas higher values represents those of cluster-glass systems [74]. Thus, the analysis described above viz., Eqs. (5), (6), and (7), suggests the formation of a cluster-glass-like state in $Gd_2Ir_{0.97}Si_{2.97}$ around 3.5 K.

E. Electrical resistivity study

To further probe the origin of different magnetic transitions observed in the system, the temperature dependence of electrical resistivity $\rho(T)$ of $Gd_2Ir_{0.97}Si_{2.97}$ is measured in zero magnetic field. The $\rho(T)$ measured in the temperature range 2–300 K during both heating and cooling is depicted in Fig. 12. No irreversibility between the heating and cooling cycle in the $\rho(T)$ behavior is observed around the observed transitions in the system, which is consistent with the absence of structural transition in the studied compound [78,79]. The resistivity is typical of a metal. A sharp drop in $\rho(T)$ is seen at ~16 K while a weak but discernible anomaly is also evident around 6.5 K. The rapid reduction of resistivity below 16 K is ascribed to the formation of a long-range ordered AFM state. A minor anomaly at $T \sim 6.5$ K is in agreement with
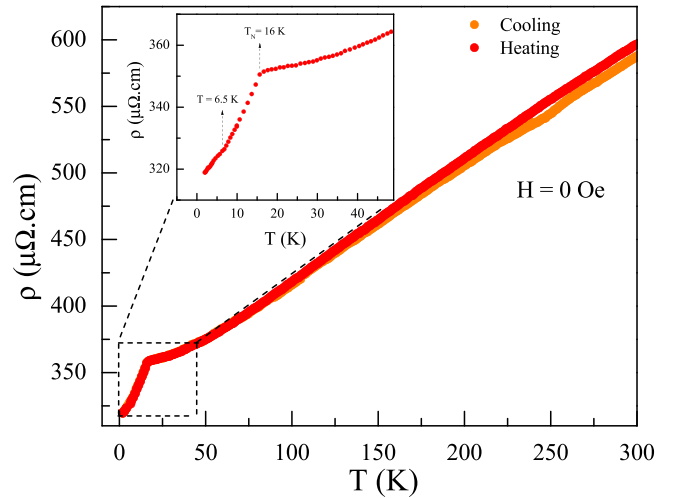

FIG. 12. Resistivity vs Temperature plot for $Gd_2Ir_{0.97}Si_{2.97}$. Inset shows the enlarged view of low temperature region.

the AC/DC magnetization and heat capacity measurements, further indicating the possibility of a ferrimagnetic-like spin reorientation. Apart from manifestation of different transitions, also evidenced in magnetic and heat capacity data, it is worthy to mention that the resistivity value for the studied compound is quite high compared to most of other R_2TX_3 systems [12,80]. The residual resistivity ratio (RRR) is also low ~1.91. It is thus plausible that the metallic character of the material is far from ideal.

F. Theoretical analysis

For insight into the magnetic and electronic structure of Gd_2IrSi_3, a number of magnetic configurations, including AFM, FiM, and FM, are considered. The unit cell of Gd_2IrSi_3 is shown in Fig. 13(a) with dotted lines highlighting a subcell used to impose different magnetic-moment orientations. A schematic of the subcell in Fig. 13(b) shows only the positions of Gd atoms, numbered from 1 to 8. Arrows ↑ and ↓ in schematic configuration I through VII show Gd moment orientations in the corresponding Gd positions. Gd2, Gd3, Gd4, Gd6, Gd7, and Gd8 belong to the $6h$ site, forming equilateral triangles in the respective planes, and Gd1 and Gd5 belong to the $2b$ site. Configurations I, II, III, and IV are AFM, where configurations III and IV are G- and C-type, respectively [81,82]. The four AFM configurations are related to each other via moment flips; for example, in the pairs of configurations (I, II), (I, III), (I, IV), (II, III), (II, IV), the first is obtained by flipping two of the moments from the second configuration. Focusing on the C-type and G-type AFM coupling because of the corresponding spin frustration, configuration I (energetically most stable among all configurations, see Table II), can be transformed from G-type AFM (III) or C-type AFM (IV) by flipping a pair of moments at positions (7,5) or (6,8), respectively. Similarly, configuration II is obtained from C-type (IV) by switching a pair of moments at (6,5). Other than these four AFM configurations, A-type AFM and FM magnetic configurations of the system are also studied (see Table II) for comparison. Both of these configurations are

TABLE II. Total energies, total magnetic moment, and energy difference ($\triangle$E) of considered magnetic configurations of the Gd_2IrSi_3 system relative to configuration I.

Configuration	Gd moments	Total energy eV/atom	Total moment μ_B/f.u.	$\triangle$E meV/atom (K)
I	↑↓↓↑↑↑↓↓	−9.5804	0	0 (0)
II	↑↓↓↑↓↑↓↑	−9.5799	0	0.5 (5.8)
III(G-type)	↑↓↓↑↓↑↑↓	−9.5803	0	0.1 (1.2)
IV(C-type)	↑↓↓↑↑↓↓↑	−9.5800	0	0.4 (4.6)
V	↑↓↓↑↑↑↓↑	−9.5797	3.48	0.7 (8.1)
VI	↑↓↓↑↑↑↑↓	−9.5800	3.48	0.4 (4.6)
VII	↑↓↓↑↓↑↑↑	−9.5797	3.48	0.7 (8.1)
A-type	↑↑↑↑↓↓↓↓	−9.5743	0	6.1 (70.8)
FM	↑↑↑↑↑↑↑↑	−9.5723	13.98	8.1 (94)

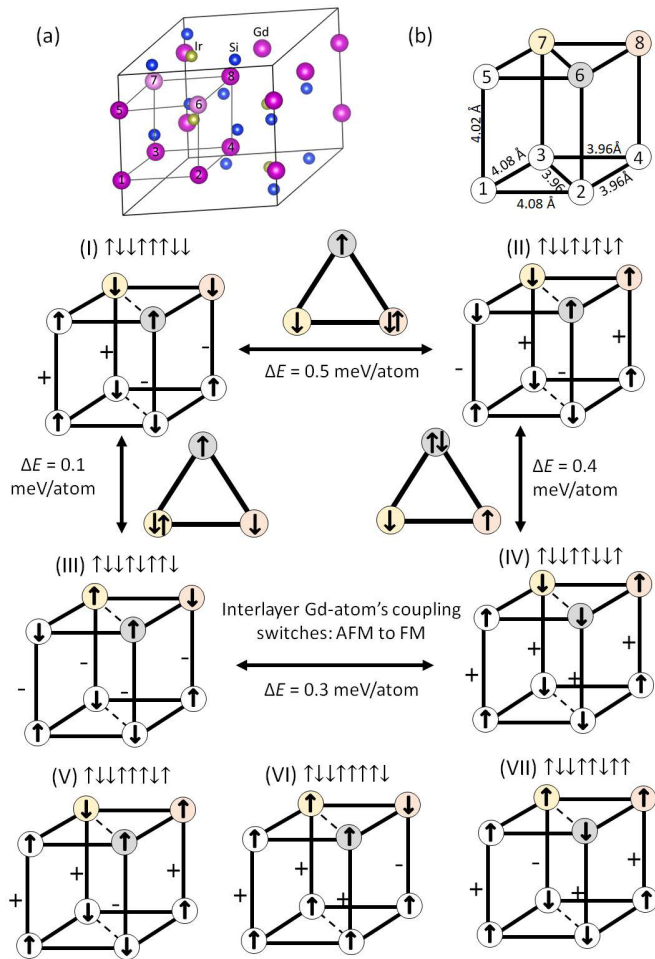FIG. 13. (a) Crystal structure of Gd_2IrSi_3, (b) schematic pseudo-primitive cell to show different Gd-moment arrangements. Schematics (I–IV) depict AFM spin configuration, while schematics (V–VII) depict FiM configurations constructed by rotating one of the moments in I, III, and IV configurations, respectively. ↑ and ↓ arrows represent the up- and down-moment directions, respectively. The signs + and − indicate the ferromagnetic (FM) and antiferromagnetic (AFM) coupling between atoms that belong to neighboring layers. The configurations III and IV are G and C-type antiferromagnets, respectively.

least favorable energetically. The signs "+" and "−" in Fig. 13 represent the interlayer FM and AFM coupling of Gd-atoms, respectively.

From Fig. 13, one can see that in the triangle of the Gd atoms mentioned above, two moments are antiparallel with each other on the triangle, while the third one gets frustrated (i.e., it may be up or down). This is well-known geometrical frustrations of AFM triangular lattice. With the choice of the direction of the third moment of the triangle at the 6h site, Gd moment on the 2b site also switches accordingly, with a very small energy difference. This indicates the possibility of competing AFM/FM ordering of Gd-moments of two different crystallographic sites. If we just focus on the triangle and rotate only one moment from the triangle and the moment at the 2b site (position 5) remains as it is, then the energy difference is still very small, but the total magnetic moment becomes 3.48 μ_B/f.u.), i.e., ferrimagnetic (FiM) coupling. Three FiM configurations (V, VI, and VII) are obtained from I, III, and IV, respectively, by rotating just one moment in the triangle that belongs to the second layer, shown in Fig. 13. Gd moment is 7 μ_B per atom, consistent with the expected g_JJ = 7 μ_B/Gd, and Ir moment is negligible in all considered AFM/FiM configurations, whereas it has a small value of 0.1 μ_B/Ir atom in FM-Gd_2IrSi_3. The energy differences between the pairs of AFM configurations (I, II), (I, III), and (II, IV) are 0.5, 0.1, and 0.4 meV/atom, respectively. The difference in energies of FiM systems V, VI, and VII with the energy of a ground-state system are small, 0.7, 0.4, and 0.7 meV/atom, respectively.

Theoretically deduced small energy differences for the rotations of one moment or a pair of them supports the possibility of strong magnetic frustrations in the system due to its geometry. As experimentally observed, due to this small energy difference between the AFM and FiM structures, the system can easily hop from AFM to FiM state as a function of temperature. Note that the energetically stable configuration-I can be achieved by rotating a pair of spins in the G-type (III) or the C-type (IV) AFM. Therefore, here we call the configuration-I a distorted G-type AFM as the energy difference between G-type and distorted G-type is the smallest i.e., 0.1 meV/atom. Therefore, the system Gd_2IrSi_3 most likely has dominating G-type AFM ground state which is competing
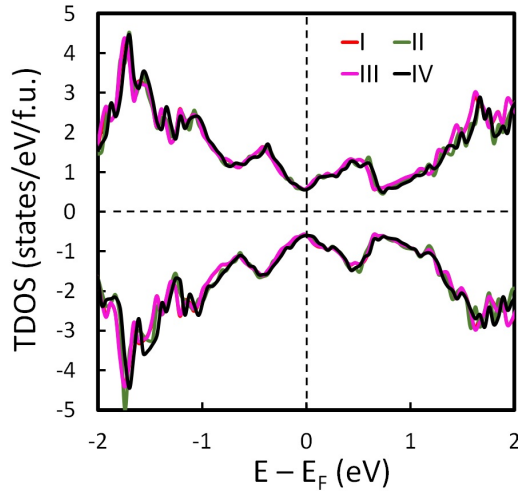
FIG. 14. The total density of states (TDOS) of the Gd$_2$IrSi$_3$ system for AFM configurations I through IV.

with C-type AFM coupling. The difference in energy between G-type [Fig. 13(III)] and C-type AFM [Fig. 13(IV)] configurations is also very small, i.e., 0.3 meV/atom indicating a competition between G-type and C-type AFM couplings.

Table II shows the total moments, total energies, and energy differences ($\triangle$E) relative to the configuration with the lowest energy, that is, the most stable AFM (I). It may be noted here, the magnetic frustrations in similar compound in the Pr$_2$Co$_{0.86}$Si$_{2.88}$ arise due to quenching of orbital moment, spin-canting, and multiple ground states [32]. In these systems, the rare-earth moments align in same direction between themselves and have canted AFM like arrangements with the moments of Co. In contrast, no canting of Gd spins is predicted in any of the considered configurations of Gd$_2$IrSi$_3$. Due to a strong frustration, multiple states are observed with competing AFM and FM nearest-neighbor interactions. FM and AFM couplings are competing both between (i) Gd atoms on the 6h site and (ii) Gd atoms on two different crystallographic sites. As experimentally observed, in the presence of such strong frustration and defects in the system, a spin-glass type of phase is formed at low temperature.

From the electronic structure, the AFM (I to IV) Gd$_2$IrSi$_3$ shows the reduction of the electronic density of states (DOS) at the Fermi energy (E$_F$), shown in Fig. 14, for both minority and majority spin channels. The local DOS at E$_F$ is around 0.5 states/eV/f.u. with a valley, the same for the majority and minority spin channels.

IV. DISCUSSION

The DC and AC magnetic susceptibility, heat capacity, and electrical resistivity measurements all reveal that Gd$_2$Ir$_{0.97}$Si$_{2.97}$ exhibits multiple magnetic transitions and a complex low-temperature magnetism. The low temperature $M(T)$ data show an AFM ordering around $\sim$16 K followed by another magnetic anomaly around $\sim$6.5 K and an additional cluster-glass phase further down the temperature ($T \leqslant 4$ K). The glassy phase appears to be magnetically reentrant in character, where the long range ordered magnetic spins structure becomes frustrated at lower temperatures.

As reported in literature for many intermetallic compounds, there are different mechanisms which can produce an additional anomaly below the AFM ordering temperature, T_N. In those antiferromagnetic systems, primarily Gd-based, additional anomalies are observed at $T^* = 0.25$–0.33 T_N [66]. Here, the additional anomaly at 6.5 K occurs at $0.4T_N$, resembling the formation of a ferrimagnetic state. According to the earlier studies anomalies below T_N are commonly due to: (i) a structural transition [68], (ii) a Schottky-like anomaly [54,69], (iii) ordering of Gd moments of different crystallographic sites at different temperatures [83,84], (iv) a magnetic ordering followed by a glassy phase transition [24], and (v) a magnetic ordering followed by a spin reorientation [85,86]. As already discussed, the transition at $\sim$6.5 K is not due to a structural distortion, nor due to a glassy phase, nor due to sequential magnetic ordering of Gd on different crystallographic sites, leaving options (ii) and (v) to consider.

Let us start with the discussion of the possible occurrence of a Schottky-like anomaly in the heat capacity data. Schottky-like anomaly involves the Zeeman splitting of $2J+1$ degenerate multiplet, where the energy positions depend on how the internal magnetic field changes with temperature. Normally, for Gd-based compounds (L = 0), the crystalline electric-field effects are negligible in the paramagnetic region, but the effect of $2J+1$ multiplet could manifest in the magnetically ordered state irrespective of long-range or short-range nature of magnetism. We have further analyzed the heat capacity data measured at zero-field in accordance with the mean-field theory (MFT) [87]. It appears that the jump in heat capacity at T_N is different for an equal moment (EM) arrangements and for amplitude modulated (AM) arrangements of the magnetic moments and MFT can explain these change in discontinuity between this two different arrangements. According to this theory, C$_{mag}(t)$ should follow the equation

$$\frac{C_{mag}(t)}{R} = \frac{3S\bar{\mu}_0^2(t)}{(S+1)t\left[\frac{(S+1)t}{3B'_S[y_0(t)]} - 1\right]}, \qquad (8)$$

$$\mu_0(t) = B_S[y_0(t)], \qquad (9)$$

$$y_0(t) = \frac{3\bar{\mu}_0(t)}{(S+1)t}, \qquad (10)$$

where, the reduced temperature, t, is defined as

$$t = \frac{T}{T_N}(H = 0). \qquad (11)$$

The jump in the heat capacity $T = T_N$ is [54,66]

$$\triangle C_{mag} = R\frac{5S(1+S)}{1+2S+2S^2} = 20.14 \text{ J/mol-K} \qquad (12)$$

Here, the Brillouin function is denoted as $B_S(y)$, $\bar{\mu}_0(t) = \mu_0(t)/\mu_{sat}(t)$ is the reduced ordered moment as a function of t at zero applied field, and μ_{sat} is the saturation spin moment. The only free parameter used in this analysis is the magnetic transition temperature. We find, however, that the theoretical description (represented by black line in Fig. 15) of an EM system overestimates the experimental data ($\triangle C_{mag} = 18$ J/mol-K). From the magnetic entropy calculation III C, we estimated that only $\sim$81% of magnetic entropy is released up to T_N, we have scaled the
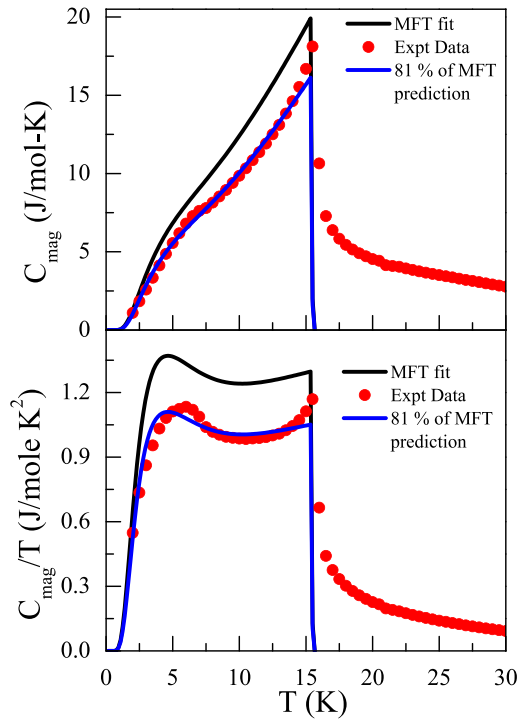
FIG. 15. The MFT predicted $C_{mag}(T)$ for $T_N = 16$ K and S = 7/2 is shown as the black solid line in upper panel. The blue curve is the generated curve assuming 81% released entropy at T_N, the lower panel shows the magnetic contribution of heat capacity as $C_{mag}(T)/T$ vs T, where also the MFT prediction for the same is shown by the black solid line, and the blue line represents the simulated MFT curve for $C_{mag}(T)/T$ vs T assuming 81% entropy released at T_N.

theoretical description accordingly and found the matching to be satisfactory (blue line in Fig. 15). We also find that the theoretical description of heat capacity is anomalous around 5 K, which is rather close to the experimental anomaly at 6.5 K. Thus, one can not completely rule out the possible linkage between the Schottky-like effect and this low-temperature anomaly. At the same time, it is worth mentioning that the Schottky-like anomaly, which is generally manifested as a broad peak in heat capacity data, is not expected to be present in the resistivity and/or magnetic susceptibility data [53,54,88]. However, in our sample, the anomaly is clearly evident not only in the $C_p(T)$, but also in $M(T)$, as well as $\rho(T)$ data. Furthermore the signature of clear domain formation in $\chi''(T, f)$ (Fig. 11) and the weak field dependence of isothermal magnetization at low-field region (H < 1 kOe) for $T \leqslant 6$ K (inset, Fig. 7) around ~6.5 K conclusively proves that the anomaly is related to a magnetic transition at that temperature rather than Schottky anomaly.

As none of the four possibilities discussed above could fully explain the anomaly at ~6.5 K, the only option remains is magnetic spin reorientation which correlates with our theoretical analysis, where we found a very large number of nearly equivalent energetically magnetic ground states, including different AFM and FiM spin arrangements. Notably,

even the ground-state energy of FM spin arrangement is not very far away either (~0.4 meV/atom) see Sec. III F. The isothermal magnetization measurements are in sync with the above possibility. Small coercivity at low temperatures could come from the glassy phase, as well as from FiM spin arrangements in 5:3 ratio (Fig. 13) and survive till ~7 K up to which the FiM structure is maintained. As the system becomes AFM, the hysteresis vanishes. We may also note here that the hysteresis behavior is also reflected in the AC susceptibility measurements that shows a nonzero value of $\chi''(T, f)$ for $T < 7$ K (Fig. 10) Thus, combining the theoretical analysis and experimental results, it appears that because of the multiple magnetic ground states of nearly equal energy, the system remains spin frustrated at the lowest temperature. As the temperature increases, the FiM spin arrangements (Fig. 2) dominates over other between 3 and 6.5 K, whereas the AFM spin structures win between 6.5 and 16 K.

V. CONCLUDING REMARKS

We have successfully synthesized a single-phase polycrystalline $Gd_2Ir_{0.97}Si_{2.97}$ by incorporating atomic vacancies. The structure supports a number of degenerate magnetic ground states and is, therefore, susceptible to magnetic frustration, as suggested by theoretical analysis. An AFM order of Gd moments ($S = 7/2$) is evident at 16 K, where the heat capacity data suggest that 81.5% of magnetic entropy is released up to T_N. The compound exhibits another transition below 6.5 K, identified as a ferrimagnetic-type spin-reorientation. As the temperature is reduced further, magnetic frustrations become dominant and a ferrimagnetic structure is succeeded by a reentrant cluster-glass phase. As revealed theoretically, magnetic frustration in this system is due to the lattice geometry and competing AFM and FM interactions that develop in the system between the nearest-neighbor moments placed in a slightly distorted triangular lattice, giving rise to highly degenerate spin configurations with nearly equivalent energies. Because of the minute energy differences between different AFM and FiM configurations, the system can easily hop between different metastable magnetic states as a function of temperature and magnetic field. The observed anomalies and multiple magnetic phase transitions in the studied $Gd_2Ir_{0.97}Si_{2.97}$ are expected to generate further attention to study and to understand the local spin textures and interactions in related materials in the context of topologically protected complex-spin textures discovered in isostructural magnetically frustrated compound Gd_2PdSi_3.

[1] A. Ramirez, Handbook Magnet. Mater. **13**, 423 (2001).

[2] A. Ramirez, Annu. Rev. Mater. Sci. **24**, 453 (1994).

[3] J. E. Greedan, J. Mater. Chem. **11**, 37 (2001).

[4] S. T. Bramwell and M. J. Gingras, Science **294**, 1495 (2001).

[5] L. Balents, Nature (London) **464**, 199 (2010).

[6] A. P. Ramirez, G. P. Espinosa, and A. S. Cooper, Phys. Rev. Lett. **64**, 2070 (1990).

[7] A. P. Ramirez, A. Hayashi, R. J. Cava, R. Siddharthan, and B. Shastry, Nature (London) **399**, 333 (1999).

[8] R. Moessner and J. T. Chalker, Phys. Rev. B **58**, 12049 (1998).

[9] K. Tomiyasu, T. Yokobori, Y. Kousaka, R. I. Bewley, T. Guidi, T. Watanabe, J. Akimitsu, and K. Yamada, Phys. Rev. Lett. **110**, 077205 (2013).

[10] Y. Machida, S. Nakatsuji, S. Onoda, T. Tayama, and T. Sakakibara, Nature (London) **463**, 210 (2010).

[11] Y. Taguchi, Y. Oohara, H. Yoshizawa, N. Nagaosa, and Y. Tokura, Science **291**, 2573 (2001).

[12] S. R. Saha, H. Sugawara, T. D. Matsuda, H. Sato, R. Mallik, and E. V. Sampathkumaran, Phys. Rev. B **60**, 12162 (1999).

[13] T. Kurumaji, T. Nakajima, M. Hirschberger, A. Kikkawa, Y. Yamasaki, H. Sagayama, H. Nakao, Y. Taguchi, T.-H. Arima, and Y. Tokura, Science **365**, 914 (2019).

[14] V. Lohani, C. Hickey, J. Masell, and A. Rosch, Phys. Rev. X **9**, 041063 (2019).

[15] V. Ukleev, K. Karube, P. Derlet, C. Wang, H. Luetkens, D. Morikawa, A. Kikkawa, L. Mangin-Thro, A. Wildes, Y. Yamasaki *et al.*, npj Quantum Mater. **6**, 40 (2021).

[16] S. Hayami and Y. Motome, Phys. Rev. B **103**, 024439 (2021).

[17] T. Nomoto, T. Koretsune, and R. Arita, Phys. Rev. Lett. **125**, 117204 (2020).

[18] N. D. Khanh, T. Nakajima, X. Yu, S. Gao, K. Shibata, M. Hirschberger, Y. Yamasaki, H. Sagayama, H. Nakao, L. Peng *et al.*, Nat. Nanotechnol. **15**, 444 (2020).

[19] M. Hirschberger, T. Nakajima, S. Gao, L. Peng, A. Kikkawa, T. Kurumaji, M. Kriener, Y. Yamasaki, H. Sagayama, H. Nakao *et al.*, Nat. Commun. **10**, 5831 (2019).

[20] S. Pakhira, C. Mazumdar, R. Ranganathan, and M. Avdeev, Sci. Rep. **7**, 7367 (2017).

[21] S. Pakhira, C. Mazumdar, A. Basu, R. Ranganathan, R. Bhowmik, and B. Satpati, Sci. Rep. **8**, 14870 (2018).

[22] D. Huo, J. Sakurai, T. Kuwai, Y. Isikawa, and Q. Lu, Phys. Rev. B **64**, 224405 (2001).

[23] S. R. Saha, H. Sugawara, T. D. Matsuda, Y. Aoki, H. Sato, and E. V. Sampathkumaran, Phys. Rev. B **62**, 425 (2000).

[24] S. Pakhira, C. Mazumdar, R. Ranganathan, S. Giri, and M. Avdeev, Phys. Rev. B **94**, 104414 (2016).

[25] D. X. Li, S. Nimori, Y. Shiokawa, Y. Haga, E. Yamamoto, and Y. Onuki, Phys. Rev. B **68**, 012413 (2003).

[26] S. Pakhira, A. K. Kundu, C. Mazumdar, and R. Ranganathan, J. Phys.: Condens. Matter **30**, 215601 (2018).

[27] S. Pakhira, C. Mazumdar, and R. Ranganathan, J. Phys.: Condens. Matter **29**, 505801 (2017).

[28] S. Pakhira, C. Mazumdar, and R. Ranganathan, Intermetallics **111**, 106490 (2019).

[29] C. Tien, L. Luo, and J. S. Hwang, Phys. Rev. B **56**, 11710 (1997).

[30] S. Majumdar, E. V. Sampathkumaran, M. Brando, J. Hemberger, and A. Loidl, J. Magn. Magn. Mater. **236**, 99 (2001).

[31] J. Leciejewicz, N. Stüsser, A. Szytula, and A. Zygmunt, J. Magn. Magn. Mater. **147**, 45 (1995).

[32] M. Kundu, S. Pakhira, R. Choudhary, D. Paudyal, N. Lakshminarasimhan, M. Avdeev, S. Cottrell, D. Adroja, R. Ranganathan, and C. Mazumdar, Sci. Rep. **11**, 13245 (2021).

[33] Y. Yasui, C. J. Butler, N. D. Khanh, S. Hayami, T. Nomoto, T. Hanaguri, Y. Motome, R. Arita, T.-H. Arima, Y. Tokura *et al.*, Nat. Commun. **11**, 5925 (2020).

[34] J. Rodríguez-Carvajal, Phys. B: Condens. Matter **192**, 55 (1993).

[35] P. E. Blöchl, Phys. Rev. B **50**, 17953 (1994).

[36] G. Kresse and J. Hafner, Phys. Rev. B **48**, 13115 (1993).

[37] J. P. Perdew, K. Burke, and M. Ernzerhof, Phys. Rev. Lett. **77**, 3865 (1996).

[38] W. Bażela, E. Wawrzynska, B. Penc, N. Stusser, A. Szytuła, and A. Zygmunt, J. Alloys Compd. **360**, 76 (2003).

[39] R. Gordon, C. Warren, M. Alexander, F. DiSalvo, and R. Pöttgen, J. Alloys Compd. **248**, 24 (1997).

[40] M. Szlawska and D. Kaczorowski, Phys. Rev. B **84**, 094430 (2011).

[41] S. Majumdar and E. V. Sampathkumaran, Phys. Rev. B **61**, 43 (2000).

[42] S. Pakhira, C. Mazumdar, R. Ranganathan, and S. Giri, Phys. Chem. Chem. Phys. **20**, 7082 (2018).

[43] S. Pakhira, C. Mazumdar, D. Choudhury, R. Ranganathan, and S. Giri, Phys. Chem. Chem. Phys. **20**, 13580 (2018).

[44] S. Pakhira, C. Mazumdar, R. Ranganathan, and S. Giri, J. Alloys Compd. **742**, 391 (2018).

[45] N. Marcano, P. A. Algarabel, L. F. Barquín, J. P. Araujo, A. M. Pereira, J. H. Belo, C. Magén, L. Morellón, and M. R. Ibarra, Phys. Rev. B **99**, 054419 (2019).

[46] S. Gupta, S. Chakraborty, S. Pakhira, C. Barreteau, J.-C. Crivello, B. Bandyopadhyay, J. M. Greneche, E. Alleno, and C. Mazumdar, Phys. Rev. B **106**, 115148 (2022).

[47] A. Pandey, A. K. Singh, S. Dan, K. Ghosh, I. Das, S. Tripathi, U. Kumar, R. Ranganathan, D. C. Johnston, and C. Mazumdar, Phys. Rev. Mater. **4**, 084411 (2020).

[48] R. Ahuja, S. Auluck, B. Johansson, and M. S. S. Brooks, Phys. Rev. B **50**, 5147 (1994).

[49] M. Colarieti-Tosti, S. I. Simak, R. Ahuja, L. Nordström, O. Eriksson, D. Åberg, S. Edvardsson, and M. S. S. Brooks, Phys. Rev. Lett. **91**, 157201 (2003).

[50] B. Harmon and A. Freeman, Phys. Rev. B **10**, 1979 (1974).

[51] I. P. Muthuselvam, R. Sankar, A. V. Ushakov, G. N. Rao, S. V. Streltsov, and F. C. Chou, Phys. Rev. B **90**, 174430 (2014).

[52] S. J. Sebastian, S. S. Islam, A. Jain, S. M. Yusuf, M. Uhlarz, and R. Nath, Phys. Rev. B **105**, 104425 (2022).

[53] N. S. Sangeetha, S. Pakhira, D. H. Ryan, V. Smetana, A.-V. Mudring, and D. C. Johnston, Phys. Rev. Mater. **4**, 084407 (2020).

[54] S. Pakhira, M. A. Tanatar, and D. C. Johnston, Phys. Rev. B **101**, 214407 (2020).

[55] Application Note 1085-152, Rev. B0, Quantum Design Inc.1 (2014), https://www.qdusa.com/siteDocs/appNotes/1085-152.pdf.

[56] E. Gopal, *Specific Heats at Low Temperatures* (Springer Science & Business Media, Cham, 2012).

[57] S. Gondh, M. M. Patidar, K. Kumar, M. P. Saravanan, V. Ganesan, and A. K. Pramanik, Phys. Rev. B **104**, 014401 (2021).

[58] N. Sluchanko, V. Glushkov, S. Demishev, A. Azarevich, M. Anisimov, A. Bogach, V. Voronov, S. Gavrilkin, K. Mitsen, A. Kuznetsov *et al.*, Phys. Rev. B **96**, 144501 (2017).

[59] M. Kundu, C. Mazumdar, R. Ranganathan, and M. De Raychaudhury, J. Magn. Magn. Mater. **489**, 165452 (2019).

[60] K. Shrestha, D. Antonio, J.-C. Griveau, K. Prokeš, P. Gaczyński, E. Colineau, R. Caciuffo, and K. Gofryk, Phys. Rev. Mater. **2**, 074401 (2018).

[61] V. K. Anand, A. K. Bera, J. Xu, T. Herrmannsdörfer, C. Ritter, and B. Lake, Phys. Rev. B **92**, 184418 (2015).

[62] L. Schoop, M. Hirschberger, J. Tao, C. Felser, N. P. Ong, and R. J. Cava, Phys. Rev. B **89**, 224417 (2014).

[63] J. Xu, V. K. Anand, A. K. Bera, M. Frontzek, D. L. Abernathy, N. Casati, K. Siemensmeyer, and B. Lake, Phys. Rev. B **92**, 224430 (2015).

[64] A. Bauer, M. Garst, and C. Pfleiderer, Phys. Rev. Lett. **110**, 177207 (2013).

[65] R. J. Goetsch, V. K. Anand, A. Pandey, and D. C. Johnston, Phys. Rev. B **85**, 054517 (2012).

[66] J. A. Blanco, D. Gignoux, and D. Schmitt, Phys. Rev. B **43**, 13145 (1991).

[67] S. Pakhira, M. A. Tanatar, T. Heitmann, D. Vaknin, and D. C. Johnston, Phys. Rev. B **104**, 174427 (2021).

[68] A. F. May, M. A. McGuire, and B. C. Sales, Phys. Rev. B **90**, 075109 (2014).

[69] S. Manni, S. L. Bud'ko, and P. C. Canfield, Phys. Rev. B **96**, 054435 (2017).

[70] N. S. Sangeetha, E. Cuervo-Reyes, A. Pandey, and D. C. Johnston, Phys. Rev. B **94**, 014422 (2016).

[71] R. P. Madhogaria, R. Das, E. M. Clements, V. Kalappattil, M. H. Phan, H. Srikanth, N. T. Dang, D. P. Kozlenko, and N. S. Bingham, Phys. Rev. B **99**, 104436 (2019).

[72] V. Tsurkan, J. Hemberger, M. Klemm, S. Klimm, A. Loidl, S. Horn, and R. Tidecks, J. Appl. Phys. **90**, 4639 (2001).

[73] C. Tien, C. H. Feng, C. S. Wur, and J. J. Lu, Phys. Rev. B **61**, 12151 (2000).

[74] J. A. Mydosh, *Spin Glasses: An Experimental Introduction* (CRC Press, Boca Raton, FL, 1993).

[75] B. Mondal, S. Dan, S. Mondal, R. Bhowmik, R. Ranganathan, and C. Mazumdar, Phys. Chem. Chem. Phys. **21**, 16923 (2019).

[76] S. Pakhira, C. Mazumdar, M. Avdeev, R. Bhowmik, and R. Ranganathan, J. Alloys Compd. **785**, 72 (2019).

[77] T. Samanta, P. A. Bhobe, A. Das, A. Kumar, and A. K. Nigam, Phys. Rev. B **97**, 184421 (2018).

[78] Y. K. Kuo, K. M. Sivakumar, H. C. Chen, J. H. Su, and C.-S. Lue, Phys. Rev. B **72**, 054116 (2005).

[79] N. Ni, S. Nandi, A. I. Kreyssig, A. Goldman, E. D. Mun, S. L. Bud'Ko, and P. C. Canfield, Phys. Rev. B **78**, 014523 (2008).

[80] S. Pakhira, R. Ranganathan, and C. Mazumdar, J. Magn. Magn. Mater. **512**, 167055 (2020).

[81] P. Das, N. S. Sangeetha, G. R. Lindemann, T. W. Heitmann, A. Kreyssig, A. I. Goldman, R. J. McQueeney, D. C. Johnston, and D. Vaknin, Phys. Rev. B **96**, 014411 (2017).

[82] A.-Y. Hu and H.-Y. Wang, J. Appl. Phys. **116**, 193903 (2014).

[83] J. L. García-Muñoz, J. Rodríguez-Carvajal, and P. Lacorre, Phys. Rev. B **50**, 978 (1994).

[84] J. Jiang, A. C. Payne, M. M. Olmstead, H.-o. Lee, P. Klavins, Z. Fisk, S. M. Kauzlarich, R. P. Hermann, F. Grandjean, and G. J. Long, Inorg. Chem. **44**, 2189 (2005).

[85] M. Dubman, E. N. Caspi, H. Ettedgui, L. Keller, M. Melamud, and H. Shaked, Phys. Rev. B **72**, 024446 (2005).

[86] Y. Y. Chen, Y. D. Yao, C. R. Wang, S. H. Lin, A. Czopnik, M. R. Ali, and J. C. Ho, Phys. Rev. B **66**, 212404 (2002).

[87] D. C. Johnston, Phys. Rev. B **91**, 064427 (2015).

[88] A. Pandey, C. Mazumdar, R. Ranganathan, and D. C. Johnston, Sci. Rep. **7**, 42789 (2017).